Nanoscale

PAPER

View Article Online
View Journal | View Issue

Cite this: *Nanoscale*, 2019, **11**, 22971

Boosting the electrocatalytic activity of amorphous molybdenum sulfide nanoflakes *via* nickel sulfide decoration†

Zheng Zheng,[a] Tong Su,[a] Jianping Shi,[b] Rui Tong,[a] Haibo Xiao,[a] Qing Zhang,[b] Yanfeng Zhang,*[b] Zhuo Wang,[c] Quan Li[d] and Xina Wang*[a]

Received 12th July 2019,
Accepted 31st October 2019

DOI: 10.1039/c9nr05916d

rsc.li/nanoscale

As a coordination polymer built of $[Mo_3S_{13}]^{2-}$ clusters, amorphous nanoscale MoS_x (a-MoS_x) is an attractive electrocatalyst for the hydrogen evolution reaction (HER) due to its abundant active sites and scalable synthesis. However, clarifying the internal catalytic mechanism and achieving even higher HER performance with scalable size are still challenging. Herein, a new hybrid catalyst of a-MoS_x flakes decorated with Ni_3S_2 nanocrystals (size < 10 nm) has been successfully synthesized on 10 × 20 cm^2-sized Ni foam by a portable hydrothermal route. As the strong interaction of $[Mo_3S_{13}]^{2-}$ clusters with Ni_3S_2 is evidenced by comprehensive binding state and Raman characterization, the polymerization effect of $[Mo_3S_{13}]^{2-}$ itself and the perfect interfaces between $[Mo_3S_{13}]^{2-}$ clusters and Ni_3S_2 are also confirmed by density functional theory calculations. These two factors greatly lower the absorption energy of hydrogen nearly to zero, leading to much improved HER activity. Current densities of 100 and 600 mA cm^{-2} are achieved at overpotentials of 181 and 246 mV, respectively, which are so far the highest values approaching practical applications. The findings of this work provide a fundamental reference about the catalytic origin of a-MoS_x based catalysts, and shed light on the practical applications of non-precious electrocatalysts for their compatibility with low cost batch production.

Introduction

Electrochemical water splitting *via* the hydrogen evolution reaction (HER) is a promising route for hydrogen generation. To decrease the overpotential and cost of water splitting, developing Earth-abundant and high-efficient HER electrocatalysts is highly demanded. Considering the high cost of the benchmark HER catalysts of Pt-based materials, great effort has been made on non-precious metal chalcogenides, phosphides, carbides, alloy and nanocarbons.[1–10] Among these alternatives, crystalline molybdenum sulfide (c-MoS_2) has attracted great attention due to its high HER activity, low cost and scalable synthesis.[11,12] The MoS_2 catalysts with various morphologies such as films, nanosheets, mesoporous foams, hollow spheres and nanoparticles have been extensively prepared,[13–18] and the overpotential was successfully decreased to ~154 mV for a current density of 10 mA cm^{-2}. However, since only the Mo terminated-edge atoms are catalytically active while those in basal planes are inactive, the exposed number of active sites of c-MoS_2 is rather limited,[19–23] together with the semiconducting character of MoS_2, making it a great challenge for the further improvement of HER with an even higher current density.

As a comparison, amorphous MoS_x (a-MoS_x) has been recently proposed as a very promising candidate for the HER due to its abundant S active sites.[24] Unlike the S–Mo–S stacking layer structure of c-MoS_2, a-MoS_x was proposed to be polymerized by $[Mo_3S_{13}]^{2-}$ clusters as building blocks, in which

[a]*Hubei Collaborative Innovation Center for Advanced Organic Chemical Materials, Hubei Key Laboratory of Ferro & Piezoelectric Materials and Devices, Faculty of Physics and Electronic Science, Hubei University, Wuhan, 430062, China. E-mail: xnw@hubu.edu.cn*
[b]*Department of Materials Science and Engineering, College of Engineering, Peking University, Beijing 100871, China. E-mail: yanfengzhang@pku.edu.cn*
[c]*State Center for Designer Low-Carbon & Environmental Materials, Zhengzhou University, Zhengzhou 450001, China*
[d]*Department of Physics, The Chinese University of Hong Kong, Hong Kong, China*

†Electronic supplementary information (ESI) available: Low-resolution TEM images of the as-prepared amorphous MoS_2-Ni_3S_2 composites attained in different regions (Fig. S1), SEM image (a) and the XRD (b) pattern of the as-prepared Ni_3S_2/NF (Fig. S2), SEM image and the XRD pattern of pure MoS_2 nanoparticles (Fig. S3), hydrogen adsorption energies at the edge and planer sites of 2H MoS_2 (0002) slabs (Fig. S4), hydrogen adsorption energies at different sites for heazlewoodite Ni_3S_2 unit cells (Fig. S5), hydrogen adsorption energies at different sites for the $[Mo_6S_{24}]$/Ni_3S_2 interface (Fig. S6), comparison of the HER performances of a-MoS_x–Ni_3S_2, Ni_3S_2 and c-MoS_2 (Table S1), faradaic efficiency obtained by the ratio between the experimental and theoretical hydrogen evolution (Fig. S7), LSV curves and EIS spectra of the as-prepared and post-annealed a-MoS_x-Ni_3S_2/NF samples (Fig. S7). See DOI: 10.1039/c9nr05916d

most of the sulfur atoms (such as apical S^{2-}, bridging S_2^{2-} and terminal S_2^{2-}) were located intrinsically as edge sites similar to those of c-MoS_2.[25–27] Accordingly, a-MoS_x possesses more catalytic activity in the HER than that of c-MoS_2,[28,29] although the origin of its activity still remains controversial.[30,31] Notably, a-MoS_x can be synthesized at a lower temperature than that of c-MoS_2,[32–36] which enables its scalable preparation. For example, MoS_x films and nanoparticles have been readily prepared on graphite or carbon-related substrates by solution processed methods such as electro-deposition, drop casting and spray coating,[28,29,32–36] and an enhanced HER performance has been observed with an overpotential of ~180 mV at 10 mA cm^{-2}.[29] Considering the practical applications in future, the scalable synthesis of catalysts on non-precious and robust metallic substrates such as Ni foam with better HER performance should be highly expected. Moreover, it has been reported that Ni-doping can not only activate the S-edge sites, reduce the free energy of hydrogen adsorption and enhance the electrical conductivity of 2H MoS_2,[37–41] but also increase the intrinsic activity of the unsaturated Mo and S sites for a-MoS_x,[32] both of which can finally promote the HER properties. Indeed, MoS_2 nanosheets on Ni_3S_2 nanoparticles, nanowires, and nanorods with a maximum sample size of 3 × 7.5 cm^2 have been prepared toward the HER;[37,42–44] however, amorphous MoS_x nanosheets decorated with Ni_3S_2 nanocrystals with an even larger sample size have been rarely reported on the NF substrate. Even less is known about the mechanism of how Ni-promotion affects the intrinsic HER activity of a-MoS_x.

In this work, a-MoS_x ultrathin flakes decorated with Ni_3S_2 nanocrystals were synthesized directly on NF with the sample size as large as 10 cm × 20 cm by a simple hydrothermal method. As $[Mo_3S_{13}]^{2-}$ nanoclusters were revealed in a-MoS_x, the strong interaction of Ni_3S_2 with $[Mo_3S_{13}]^{2-}$ was disclosed by Raman and XPS spectra. The modification of Ni_3S_2 on the free energy of hydrogen adsorption (ΔG_{H^*}) of $[Mo_3S_{13}]^{2-}$ was demonstrated by density functional theory (DFT) calculations, which finally leads to the high HER activity with overpotentials of 181 and 246 mV to reach the current of 100 and 600 mA cm^{-2}, respectively. Our findings clarify the catalytic origin of both the $[Mo_3S_{13}]^{2-}$ nanoclusters and the effect of Ni_3S_2 on the composites.

Experimental

Materials

Sodium molybdate dihydrate (chemical formula: $Na_2MoO_4{\cdot}2H_2O$, analytical reagent), thioacetamide (TAA, chemical formula: CH_3CSNH_2, analytical reagent), oxalic acid dihydrate (chemical formula: $C_2H_2O_4{\cdot}2H_2O$, analytical reagent), nickel foam (purity: 99.8%, thickness: 1.7 mm), all other materials and chemicals were products of Sinopharm Chemical Reagent Co. Ltd.

Synthesis of a-MoS_x-Ni_3S_2/NF. Amorphous MoS_x-Ni_3S_2 was synthesized by a NF assisted one-step hydrothermal method, in which NF serves as both a support and a Ni source. Simply, a piece of Ni foam (10 cm × 20 cm) was cleaned with distilled water and alcohol for 10 minutes, was rolled up and then immersed in a Teflon-lined stainless-steel autoclave containing 400 mL aqueous precursor solution. The precursors consist of 1 mM sodium molybdate, 2 mM thioacetamide and 0.125 mM oxalic acid. Then the autoclave was put into an electric oven and heated at 200 °C for 10 h. After cooling down to room temperature, a black layer of a MoS_x-Ni_3S_2 composite formed on NF. Similar composites were also prepared by varying the concentration of sodium molybdate from 0.5 mM to 1.5 mM with other parameters unchanged. For comparison, pure Ni_3S_2/NF was prepared by a similar hydrothermal method except the addition of sodium molybdate. In addition, a Pt/C electrode was prepared by the method as reported in our previous work.[45]

Synthesis of MoS_2 powder and MoS_2/NF. MoS_2 powder was prepared by the following hydrothermal method. Typically, 0.5 mM of sodium molybdate and 4 mM of thioacetamide were dissolved in 60 mL distilled water under vigorous stirring for 10 minutes to form a homogeneous solution. Then 0.25 mM oxalic acid was added under vigorous stirring for another 10 minutes. The precursor solution was then transferred into a Teflon-lined stainless steel autoclave and heated at 200 °C for 10 h. After drying at 60 °C for 5 h, black MoS_2 powders can be obtained. MoS_2/NF was prepared by drop-casting the MoS_2 powder solution (6 mg mL^{-1} in ethanol) on a piece of Ni foam (2 cm × 2 cm).

Characterization. The morphology and structure were studied by field emission scanning electron microscopy (SEM, JSM-7100F, JEOL), X-ray diffraction (XRD, Bruker D8, Cu Kα (λ = 1.54056 Å)) and transmission electron microscopy (TEM, FEI Tecnai 20) equipped with STEM and energy dispersive X-ray spectroscopy (EDS). Chemical compositions and states were characterized by X-ray photoelectron spectroscopy (XPS) measurements (XPS, Escalab 250Xi) with Al Kα radiation. Raman spectra experiments were carried out using a HORIBA iHR 550 micro-Raman spectrometer.

Electrochemical measurements. The electrochemical measurements including linear sweep voltammetry (LSV), cyclic voltammetry (CV) and Electrochemical Impedance Spectroscopy (EIS) were performed in a three-electrode system using a CHI 760E (Shanghai Ch Instrument Company, China) and a CS350H (Wuhan Corrtest Instrument Company, China) electrochemical analyzer at room temperature. The as-prepared sample, Pt foil and Ag/AgCl electrode were used as the working, counter and reference electrode, respectively. An ion-exchange membrane was used in the reactor to avoid possible Pt contamination.[46] The electrolyte was 1 M KOH aqueous solution. CdI tests were conducted within the range of 0.1–0.3 V (*vs.* RHE) at rates from 20 to 140 mV s^{-1}. The scan rate for LSV curves was kept at 2 mV s^{-1}. The EIS was measured from 100 kHz to 0.1 Hz at an overpotential of 110 mV. All data were processed with 90% iR compensation. The potentials *vs.* the Ag/AgCl electrode were converted to those *vs.* the reversible hydrogen electrode (RHE) using the equation $E_{RHE} = E_{Ag/AgCl} + 0.1976 + 0.0591 \times pH$.

DFT calculations. All theoretical calculations were carried out within the frame-work of DFT using the Vienna *Ab initio* Simulation Package (VASP) with the projector-augmented wave potential.[47] Generalized gradient approximation (GGA) with the Perdew–Burke–Ernzerhof (PBE) functional was adopted to approximate the exchange–correlational effects.[48] The kinetic energy cutoff was set to 450 eV for the plane-wave basis restriction, and an energy criterion of 10^{-5} eV was reached for a self-consistency cycle. The structural optimization was continued until the residual forces have converged to less than 0.01 eV $Å^{-1}$.

Results and discussion

A hydrothermal method is a facile strategy for the synthesis of MoS_2-Ni_3S_2 hetero-structures, and in most cases crystalline MoS_2 were grown on a Ni_3S_2 matrix such as nanoparticles, nanowires, and nanorods.[37,42–44] Herein, by changing the type and concentration ratio of the sulfur and molybdenum source, an inverse structure of Ni_3S_2 nanocrystals on the amorphous MoS_x nanosheet matrix was realized with a sample size of 10 cm × 20 cm *via* a NF-assisted hydrothermal growth method as shown in Fig. 1a and b. Notably, the NF served as both a substrate and an effective Ni source. The Ni_3S_2 nanocrystals were synthesized by reactions (1) and (2), while MoS_x nanoflakes formed *via* reactions (1) and (3) as shown below:

$$CH_3CSNH_2 + 2H_2O \rightarrow CH_3COONH_4 + H_2S \quad (1)$$

$$2H_2S + 3Ni \rightarrow Ni_3S_2 + 2H_2 \quad (2)$$

$$(x+1)H_2S + MoO_4^{2-} \rightarrow MoS_x + SO_4^{2-} + (x+1)H_2 \quad (3)$$

Since it was reported that crystalline MoS_2 formed at ≥350 °C,[28,29] here, the low growth temperature (200 °C) together with the high-pressure condition caused by the reactive H_2S gas contributes to the formation of amorphous MoS_x flakes. From the phtotograph of the whole sample (Fig. 1b), large-scale growth of a-MoS_x-Ni_3S_2 composites can be realized with a loading mass of 5.7 mg cm^{-2}. As presented by the top- and side-view SEM images (Fig. 1d–f), uniform nanoflakes with a thickness of ~2.4 μm were grown on Ni foam. The high-resolution SEM image exhibits that the nanoflakes are highly curly and crossed with each other, leading to a hollow sphere-like morphology with an average size of ~85 nm. In order to detect the chemical constituent of such nanoflakes, the energy dispersive X-ray (EDX) measurement was performed on the as-grown sample (Fig. 1g). Typical Ni, Mo and S signals are clearly observed in the nanoflakes with an atom ratio of ~4 : 5 between Mo and Ni. From the XRD pattern of heazlewoodite Ni_3S_2 (PDF No. 44-1418) (Fig. 1c), except the signal from NF, diffraction peaks of (101), (110), (003), (202), (211) and (122) planes could be detected at 22.08°, 31.38°, 38.10°, 44.45°, 50.40° and 55.45°, respectively. No obvious diffraction peaks of MoS_2 were found, suggesting its amorphous nature. It should be noted that it is difficult to distinguish the Ni_3S_2 nanocrystals from the flakes in SEM images.

TEM and scanning TEM (STEM) measurements were performed to investigate the detailed microstructure and elemental distribution. From the low-magnification TEM image (Fig. 2a), thin a-MoS_x-Ni_3S_2 nanoflakes can be observed. By measuring the edge regions of no less than 20 flakes (ESI Fig. S1†), it can be deduced that the nanoflakes have an

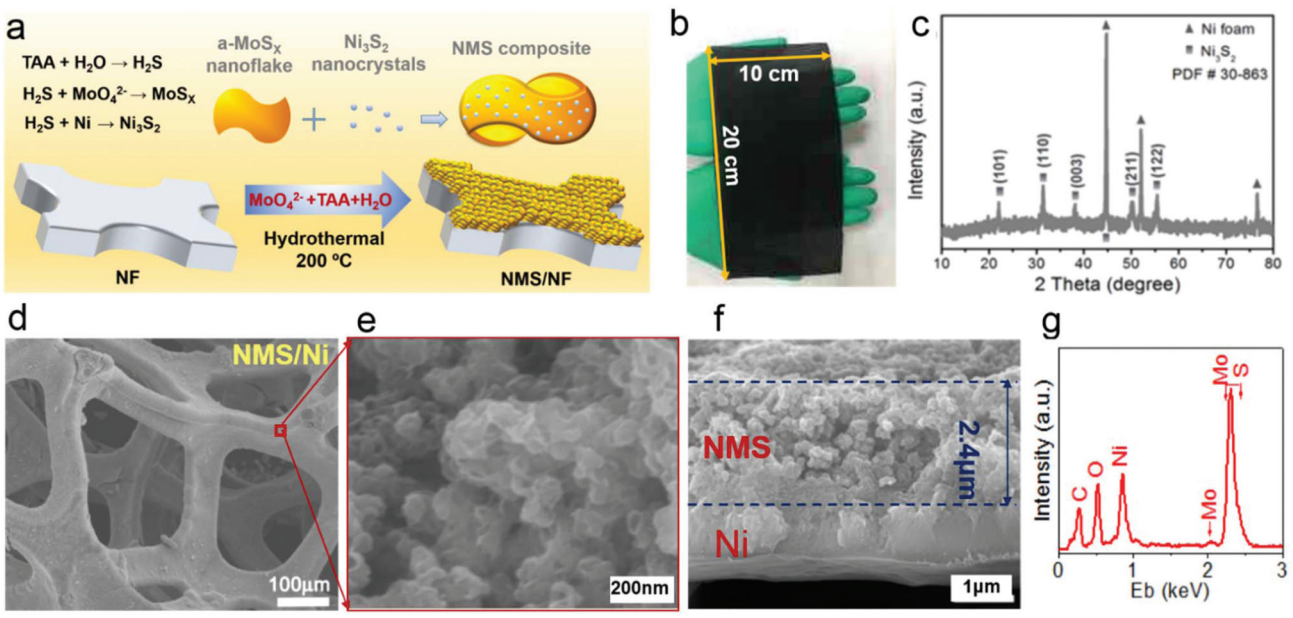

Fig. 1 Hydrothermal synthesis, morphology and crystallinity characterization of the a-MoS_x-Ni_3S_2 composite on Ni foam with the sample size of 10 cm × 20 cm. (a) Schematic illustration of the hydrothermal growth process, during which the Ni foam served as both the Ni source and support for the composite. (b) Photograph of the a-MoS_x-Ni_3S_2 sample synthesized on 10 cm × 20 cm-sized Ni foam. (c) XRD pattern showing the heazlewoodite phase of Ni_3S_2 and the amorphous nature of MoS_x. (d–f) Top-view and cross-sectional SEM images, where a-MoS_x-Ni_3S_2 is abbreviated as "NMS". (g) is the EDX spectrum indicating the existence of Ni, Mo and S in a-MoS_x-Ni_3S_2 flakes.

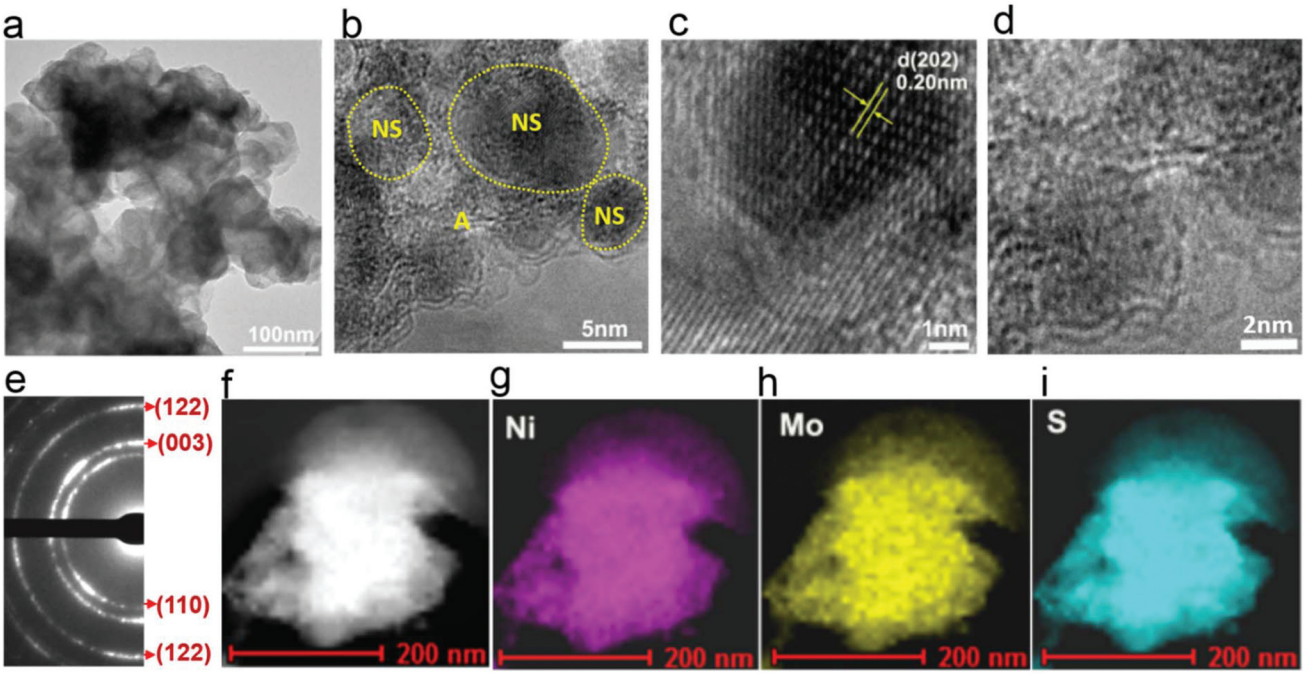

Fig. 2 Microstructure and elemental distribution of a-MoS_x-Ni_3S_2 hybrid nanoflakes. (a and b) Different magnification TEM images exhibiting the co-existence of Ni_3S_2 (denoted as NS) nanocrystals and the amorphous MoS_x structure. (c and d) High-resolution TEM images of Ni_3S_2 and the amorphous domains captured in region A of (b). (e) SAED pattern showing the amorphous nature of MoS_x and polycrystalline Ni_3S_2. (f–i) STEM HAADF image and the corresponding Ni K, Mo K and S K elemental mapping images, exhibiting the uniform distribution of Ni_3S_2 in a-MoS_x.

average thickness of less than 5 nm. The high-resolution TEM images (Fig. 2b–d) exhibit that the nanoflakes with plenty of amorphous domains are decorated with nanocrystals with the size of 2–10 nm. An average size of ~7 nm can be estimated from the particle size distribution image in ESI Fig. S2.† The lattice spacing of the crystals is estimated as ~0.20 nm, matching the *d*-spacing of the (202) planes of Ni_3S_2. In the TEM image (Fig. 2d) captured from region A in Fig. 2b, although some layer-like structure appears at the edge of the flake, no lattice planes related with crystalline MoS_2 can be resolved in the amorphous domains. At the same time, only one set of diffractive rings of heazlewoodite Ni_3S_2 (110), (003) and (122) planes had been detected in the SAED pattern (Fig. 2e), which also excludes the possibility of crystalline 2H MoS_2 and the cubic phase of Ni. The HAADF (high-angle annular dark-field) image (Fig. 2f) and the corresponding EDX mappings (Fig. 2g–i) of Ni, Mo and S indicate the uniform distribution of Ni_3S_2 in a-MoS_x domains.

Raman spectroscopy is a powerful tool to probe the local structure and phonon mode of a long range order that can't even be detected by XRD. The building block nature of the $[Mo_3S_{13}]^{2-}$ cluster in a-MoS_x and the interaction with Ni_3S_2 were evidenced by Raman spectra (Fig. 3a). For a-the MoS_x-Ni_3S_2 composite, Ni–S vibrations can be observed at or within 176–206, 220, 244, 298 and 347 cm^{-1}, respectively.[49,50] Compared to pure Ni_3S_2 (detailed morphology and XRD results can be found in ESI Fig. S3†), the frequency slightly shifted to a low wavenumber, indicating the strong influence of a-MoS_x on the lattice vibration of Ni_3S_2. Meanwhile, distinctive vibrations of Mo–S linkages (ν(Mo–S) at 285 and 342 cm^{-1}, and $\nu(Mo_3–S)$ at 450 cm^{-1}) and bridging/shared disulfide ($\nu(S–S)_{br/sh}$ at 562 cm^{-1}) were clearly observed, suggesting the presence of $[Mo_3S_{13}]^{2-}$ clusters in a-MoS_x.[28,29] Compared with the strong E^1_{2g} (380 cm^{-1}) and A_{1g} (406 cm^{-1}) vibrations typically for well-crystalline MoS_2,[51,52] the amorphous structure of MoS_x has very weak in-plane Mo–S vibration (E^1_{2g} mode) and edge phonon mode at 372 and 482 cm^{-1}, respectively.

The chemical states of pure Ni_3S_2, MoS_2 and a-MoS_x-Ni_3S_2 composites were further characterized by X-ray photoelectron spectroscopy (XPS) fine scans as shown in Fig. 3b–d. The binding energies of Mo^{4+} $3d_{5/2}$ at 228.6 eV and $3d_{3/2}$ at 232.1 eV, and S $2p_{1/2}$ at 162.5 eV and $2p_{3/2}$ at 161.5 eV are clearly observed for MoS_2 nanoparticles (for detailed information see ESI Fig. S4†). For the composites of a-MoS_x and Ni_3S_2, typical Mo^{4+} $3d_{5/2}$ and $3d_{3/2}$ peaks at 228.9 eV and at 232.3 eV, together with Ni^{2+} $2p_{1/2}$ and $2p_{3/2}$ at 873.5 and 855.8 eV can be found. In the lower energy region of the S 2p spectrum, besides the binding energy of S^{2-} from Ni_3S_2 at 162.7 and 161.6 eV (peaks V and VI), obvious signals of the S species from the $[Mo_3S_{13}]^{2-}$ clusters can be detected, including apical S^{2-} and/or bridging S_2^{2-} at 164.4 (peak I) and 163.3 eV (peak II), and the unsaturated S^{2-} and/or terminal S_2^{2-} doublet peaks at 163.0 (peak III) and 162.3 eV (peak IV), respectively. This further proves the hybrid of Ni_3S_2 and $[Mo_3S_{13}]^{2-}$. In addition, compared with pure MoS_2 and Ni_3S_2, although the Ni peaks of the composites remain unchanged, the Mo 3d peaks have a positive shift of about 0.2–0.3 eV relative to those of MoS_2, which may be caused by the more S atoms that bond

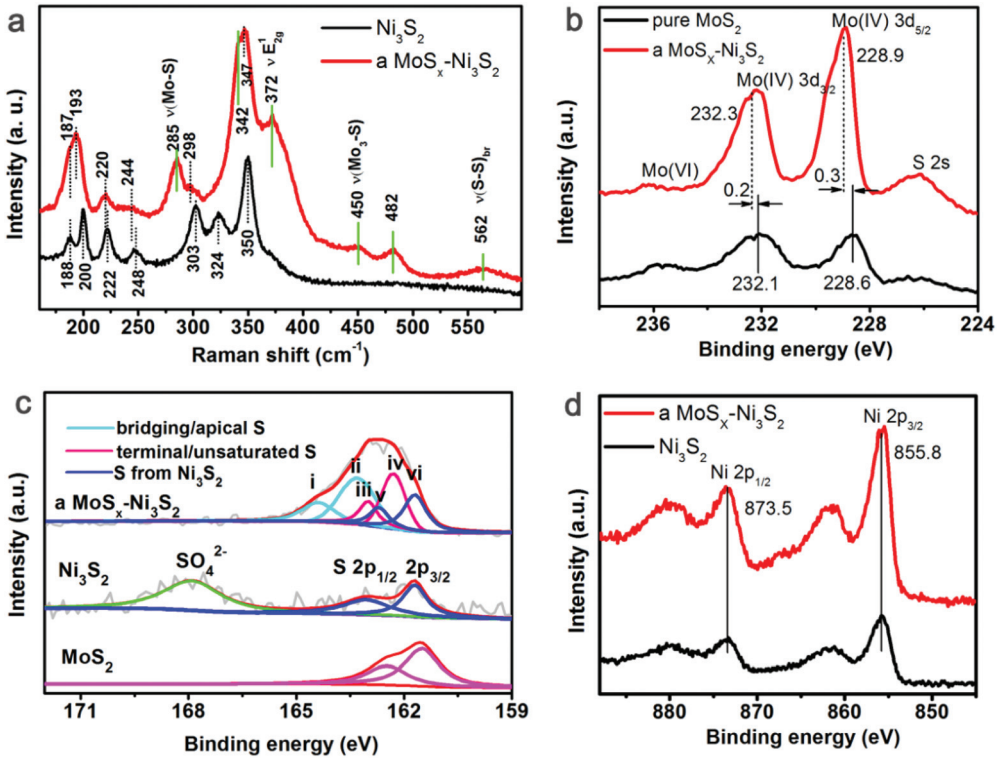

Fig. 3 Raman and XPS characterization of the interaction of a-MoS_x with Ni_3S_2. (a) Raman spectrum of the MoS_x-Ni_3S_2 composite and Ni_3S_2, in which an obvious shift of Ni–S vibration (indicated by black dotted lines) can be found after composition with a-MoS_x, and the green lines show the typical vibrations of Mo_3S_{13}. (b) Mo 3d XPS spectra of pure MoS_2 and the MoS_x-Ni_3S_2 composite exhibiting obvious shifts of the bonding energy. (c) S 2p XPS spectra of the composite, pure Ni_3S_2 and MoS_2, where peaks I–II and III–IV can be assigned to the bridging/apical and terminal/unsaturated S atoms of $[Mo_3S_{13}]^{2-}$, while peak V comes from Ni_3S_2. (d) XPS fine spectra of Ni 2p of pure Ni_3S_2 and the composite.

with Mo in Mo_3S_{13} clusters and/or the strong electronic interaction of Mo_3S_{13} with Ni_3S_2 nanocrystals.

Recent theoretical calculations demonstrated that there were two opposite origins of the active sites of discrete $[Mo_3S_{13}]^{2-}$ clusters (the structure model is shown in the left panel of Fig. 4a), one was bridging S_2^{2-}, and the other was terminal S_2^{2-} ligand.[27,28] In fact, for a-MoS_x prepared either as nanoflakes or as nanoparticles, $[Mo_3S_{13}]^{2-}$ clusters will connect with each other by sharing at least one of the terminal S_2^{2-} ligands, thus forming a fourth type of S atoms, *i.e.*, shared S_2^{2-} as shown in the middle panel of Fig. 4a.[26,29] Although the activity of bridging and terminal S was discussed, the activity of shared S has been rarely addressed, even less study has been done for the effect of Ni_3S_2 on the activity of $[Mo_3S_{13}]^{2-}$ cluster. To justify the catalytic activity of a-MoS_x and its composition with Ni_3S_2, DFT calculations were performed. As a reference, both the heazlewoodite Ni_3S_2 and 2H MoS_2 slab were also discussed (the calculation details can be found in ESI Fig. S5 and S6†). The descriptor of ΔG_{H^*} was calculated to evaluate the HER activity. In general, a value approaching zero suggests superior HER properties due to the optimal balance between the absorption and desorption of hydrogen species on active sites.[14] As shown in Fig S5,† the hydrogen adsorption energies are 0.47 and 1.06 eV at the S and Ni sites in the exposed Ni_3S_2 (101) plane. In Fig. 4b, the values for the Mo-edge, S-edge and basal-plane of 2H MoS_2 are 0.06, −0.45 and 2.13 eV, respectively, well consistent with the reported results.[53] For discrete $[Mo_3S_{13}]^{2-}$ clusters, the values for the apical, terminal and bridging S are 2.26, 1.20, and 0.66 eV, respectively, which decrease greatly to 2.13, 0.60, and 0.44 eV for the $[Mo_6S_{24}]^{2-}$ cluster. It is noticeable that the shared-S in $[Mo_6S_{24}]^{2-}$ cluster has a value of only −0.02 eV, which is much closer to zero than both the Mo-edge of 2H MoS_2 and the S atoms of $[Mo_3S_{13}]^{2-}$, suggesting its superior activity than the latter two. Since a-MoS_x was formed by polymerization of $[Mo_3S_{13}]^{2-}$ clusters, during which process terminal S atoms are shared by two adjacent $[Mo_3S_{13}]^{2-}$ clusters, the shared S can thus be thought as active sites for the HER due to the low value.

When Ni_3S_2 was introduced into a-MoS_x, a simplified model of $[Mo_3S_{13}]^{2-}$ cluster-interfacing with the Ni_3S_2 (101) plane was built based on the TEM results (right panel of Fig. 4a). Compared to the discrete $[Mo_3S_{13}]^{2-}$ cluster, a notable decrease in the ΔG_{H^*} values can be found after $[Mo_3S_{13}]^{2-}$ were interfaced with Ni_3S_2. In particular, the ΔG_{H^*} values of bridging and terminal S are only −0.05 and 0.24 eV, respectively, suggesting their main roles as active sites. The modified absorption free energy is much closer to zero than both the discrete $[Mo_3S_{13}]^{2-}$ cluster and those modulated *via* the catalyst–support interaction of Cu and the graphene support.[28,34]

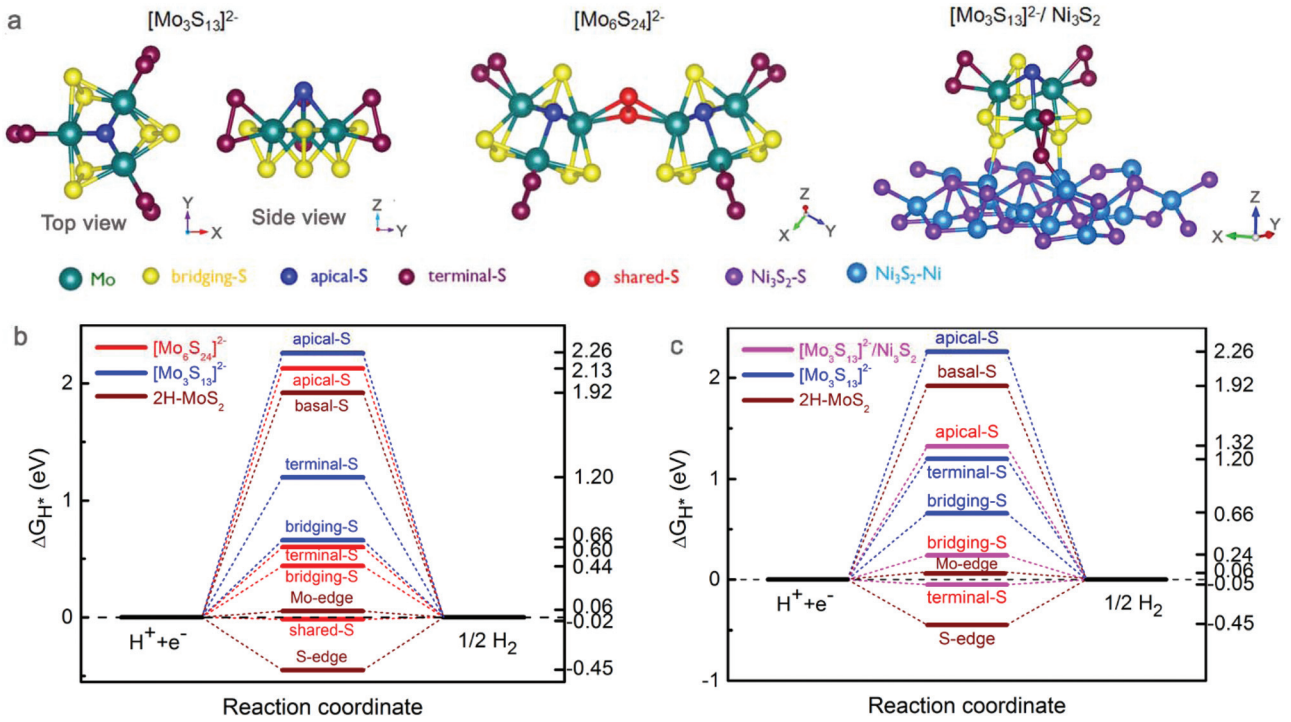

Fig. 4 Structure models and hydrogen adsorption free energies at different sites of $[Mo_3S_{13}]^{2-}$, $[Mo_6S_{24}]^{2-}$ clusters and at the $[Mo_3S_{13}]/Ni_3S_2$ interface. (a) Structure models; (b and c) the diagrams for hydrogen adsorbed at different sites of the clusters, composite and 2H MoS_2 slab.

At the same time, when the $[Mo_6S_{24}]^{2-}$ cluster is interfaced with Ni_3S_2 (for detailed information see ESI Fig. S7†), the ΔG_{H^*} of terminal S falls within −0.03 to −0.06 eV, while the shared S and 60% bridging S atoms have $|\Delta G_{H^*}|$ less than 0.26 eV. The results also indicate that the terminal S and most part of bridging S atoms of the $[Mo_6S_{24}]^{2-}$ cluster can be activated by interfacing with Ni_3S_2. Accordingly, it is deduced that the catalytic activity of a-MoS_x can be further enhanced by the increased density of active sites *via* interfacing with Ni_3S_2.

The HER performance of a-MoS_x-Ni_3S_2 composites was confirmed by the different-current range LSV curves shown in Fig. 5a and b. The polarization curves of MoS_2/NF, Ni_3S_2/NF, NF and Pt/C electrodes are also given as a comparison. As shown in Fig. 5a and b, a-MoS_x-Ni_3S_2/NF synthesized with the molar ratio of the Mo/S precursor of 1 : 2 shows remarkable catalytic properties with currents of 10, 100 and 600 mA cm^{-2} at 109 (η_{10}), 181 (η_{100}) and 246 (η_{600}) mV, respectively, superior than those of MoS_2/NF, Ni_3S_2/NF and NF. It should be noted that the performance degradation of Pt/C in the base electrolyte at a high current density comes from the detachment of Pt catalysts from the electrode or the increased bubbles on the electrodes. The linear portions of the Tafel plots in Fig. 5c were fitted to the Tafel equation ($\eta = b \log j + a$, where j is the current density and b is the Tafel slope), yielding Tafel slopes of 64.3, 111.1, and 183.5 mV dec^{-1} for a-MoS_x-Ni_3S_2, MoS_2 and Ni_3S_2/NF, respectively. The Tafel slope of a-MoS_x-Ni_3S_2 and MoS_2 locates within 40–116 mV dec^{-1}, indicating the Volmer–Heyrovsky HER mechanism in alkaline media.[54] The Pt/C electrode still shows the benchmark Tafel slope of 30.3 mV dec^{-1}. Fig. 5d lists the Tafel slope and η_{10} values of recently reported MoS_x and Ni_3S_2-based catalysts (detailed information can be found in ESI Table S1†), where the blue and pink region denote the performance obtained in the acidic and basic electrolyte, respectively. Compared to $[Mo_3S_{13}]$,[26,32] pure and Co/Ni-doped 2H MoS_2 nanosheets or nanospheres working in acidic media,[17,55–59] the a-MoS_x-Ni_3S_2 composite has a much lower overpotential. This composite also exhibits a superior Tafel slope to those of Ni_3S_2,[56] 2H-MoS_2@Ni,[40] 2H-MoS_2-Ni_3S_2,[37] MoS_2-NiCo LDH and MoO_x-Ni_3S_2 composites which were measured in alkaline media.[60,61] Although the low-current activity of a-MoS_x-Ni_3S_2 is a little inferior than the Ni-doped MoS_2 on carbon cloth,[62] the composites exhibit higher performance in the higher-current range, in which the overpotential is as low as 246 mV when working at 600 mA cm^{-2}, nearly the best value up to now. Moreover, the large sample size (10 cm × 20 cm) makes it possible for future application. Compared to the alkaline electrolyte, the a-MoS_x-Ni_3S_2 composite shows inferior HER properties in H_2SO_4 while very poor activity in phosphate buffered saline (PBS) solution (detailed information can be found in ESI Fig. S8†).

The charge transfer resistance (R_{CT}) was also evaluated by the semicircle radius of the Nyquist plots from the EIS spectra (Fig. 5e). Compared with Ni_3S_2 (45.24 Ω) and MoS_2 nanoparticles (16.88 Ω), the a-MoS_x-Ni_3S_2 hybrid has a much smaller R_{CT} (0.93 Ω), suggesting promoted charge transfer upon the composition of a-MoS_x and Ni_3S_2. By changing the molar ratio of the Mo/S precursor in synthesizing the hybrids (detailed information can be found in ESI Fig. S9†), it is found

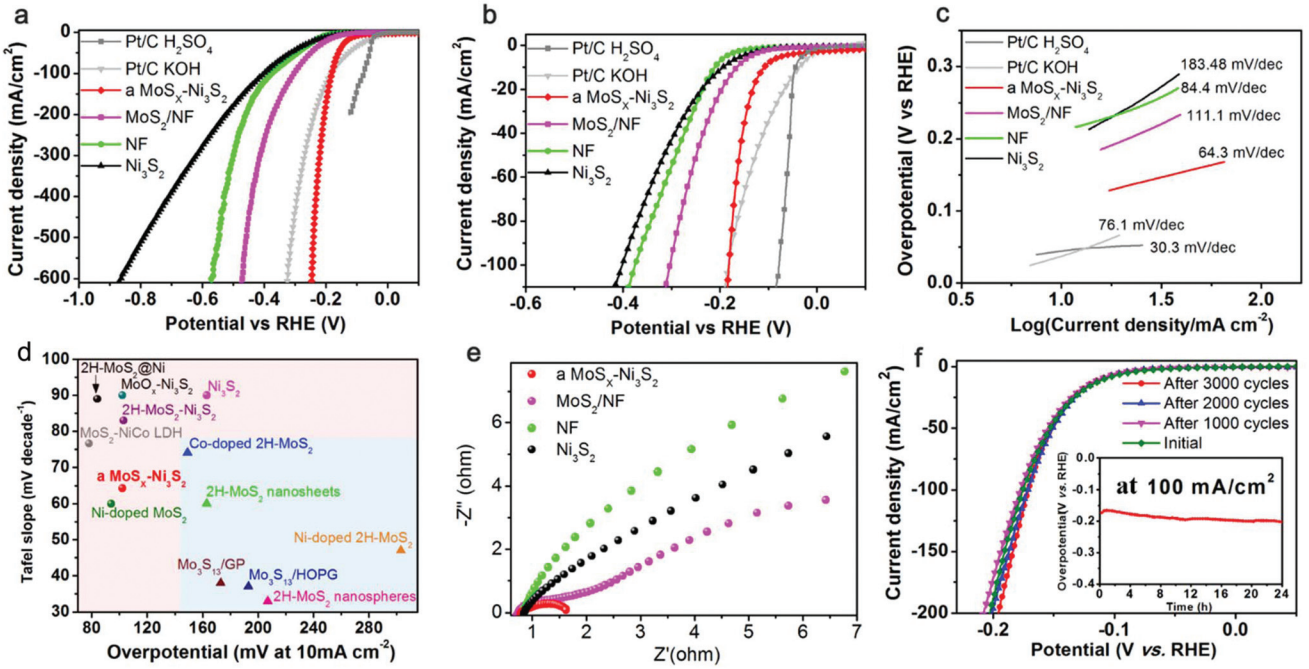

Fig. 5 Electrochemical and durability properties of the a-MoS_x-Ni_3S_2 composite. (a and b) Different-current range LSV curves, (c) Tafel plots and (e) Nyquist plots of the as-prepared a-MoS_x-Ni_3S_2, Ni_3S_2/NF, MoS_2/NF and NF in 1 M KOH. Note that (b) is the enlarged LSV curves from part (a). The data of the Pt/C electrode measured in respective KOH and H_2SO_4 are also provided for reference. (d) The comparison of Tafel slopes and overpotentials at 10 mA cm^{-2} between the a-MoS_x-Ni_3S_2 composite and other typical molybdenum sulfides. The blue and pink regions denote the performance obtained in acidic and basic media, respectively. (f) The LSV curve obtained before and after 1000, 2000 and 3000 CV cycles, inset (f) shows the time-dependence of the overpotentials at a static current density of 100 mA cm^{-2} for 24 h.

that the hybrid shows the highest HER performance with the Mo/S precursor ratio of 1 : 2; a lower or higher Mo precursor concentration will cause the degeneration of the performance. According to the CV curves in ESI Fig. S10,† a double-layer capacitance (C_{dl}) of 234 mF cm^{-2} can be deduced, leading to a high electrochemically active surface area (ECSA) of 5.85×10^3 cm^2 and a moderate TOF value of ~0.067 H_2 s^{-1}. Furthermore, the composite shows a CV cycle-enhanced HER activity. As shown in Fig. 5f, the overpotential initially increases and then decreases slightly with the CV cycle. After 3000 cycles, the overpotentials required to achieve the current density of 100 and 200 mA cm^{-2} decrease by 4 and 7 mV, respectively, compared to the as-prepared sample. Moreover, there is a negligible change in the microstructure and composition of the sample after 3000 cycles (ESI Fig. S11†). The long-term galvanostatic measurement (the inset of Fig. 5f) also suggests the good electrocatalytic stability of the sample, in which the overpotential only increases by 27 mV with negligible morphology change after measurement at 100 mA cm^{-2} for 24 h. Additionally, a faradaic efficiency of 94% was realized when the as-prepared composites worked at a constant current of 20 mA cm^{-2} (Fig. S12†).

The high HER activity of a-MoS_x-Ni_3S_2/NF can be attributed to three main reasons. Firstly, the composition with Ni_3S_2 can activate the S atoms of a-MoS_x for the HER by lowering the ΔG_{H^*}, and then increase the number of catalytically active species. Secondly, thanks to the ultrathin nanoflake morphology of a-MoS_x and the small size of Ni_3S_2 nanocrystals (<10 nm), a large ECSA with a high density of active sites can be realized for the hydrogen adsorption and evolution reaction. Thirdly, the 3D network of Ni foam promotes both the transport of electrons and the release of hydrogen bubbles. It was found that high-temperature annealing would deteriorate both the HER activity and charge transfer properties. As shown in Fig. S13,† the overpotential and R_{CT} increased gradually with annealing at 400 °C. After annealing at 500 °C, η_{10} increased from 101 mV to 169 mV and R_{CT} increased from 0.93 Ω to 7.52 Ω. Since a-MoS_x to c-MoS_2 phase transformation happened at 350 °C,[25–27] the deterioration can be understood by the reduced active sites (bridging/terminal-S) of a-MoS_x during the crystallization process.

Conclusions

In summary, a-MoS_x ultrathin nanoflake-Ni_3S_2 nanocrystal composites were synthesized directly on an NF substrate with a sample size of 10 cm × 20 cm *via* a portable hydrothermal method. The a-MoS_x matrix was found to consist of $[Mo_3S_{13}]^{2-}$ nanoclusters, and its interaction with the Ni_3S_2 nanocrystals (size < 10 nm) was confirmed by obvious bonding energy shifts. DFT simulations revealed that besides the active sites of shared S in the a-MoS_x matrix, after composition with Ni_3S_2, the bridging and terminal S will become catalytically active

due to the lowered ΔG_{H^*} values nearly to zero. The enhanced native activity with increased species of active sites, together with the high active density due to the large specific surface area, and the 3D network of well conductive and scalable Ni foam, endowed the composites with excellent HER activity, and a η_{600} of 246 mV was achieved. The findings of this work provide a fundamental reference about the catalytic origin of a-MoS_x based catalysts, and shed light on the practical applications of non-precious electrocatalysts for their compatibility with low cost batch production.

Conflicts of interest

The authors declare no conflict of interest.

Acknowledgements

This work was supported by the National Natural Science Foundation of China (No. 51472080, 51602094, 11104097), the Open Research Fund Program of the State Key Laboratory of Low-dimensional Quantum Physics (No. KF201705), and the Excellent Youth Foundation of Hubei Province (No. 2017CFA038). We thank Prof. Zhongbin Huang and Dr Hui Yang from the Center for Computational Science, HUFPET, for helping with DFT calculations.

References

1 B. Radisavljevic, A. Radenovic, J. Brivio, V. Giacometti and A. Kis, *Nat. Nanotechnol.*, 2011, **6**, 147–150.
2 O. Lopez-Sanchez, D. Lembke, M. Kayci, A. Radenovic and A. Kis, *Nat. Nanotechnol.*, 2013, **8**, 497–501.
3 A. R. Kucernak and V. N. Sundaram, *J. Mater. Chem. A*, 2014, **2**, 17435–17445.
4 J. Jia, T. Xiong, L. Zhao, F. Wang, H. Liu, H. R. Hu, J. Zhou, W. Zhou and S. Chen, *ACS Nano*, 2017, **11**, 12509–12518.
5 A. Anastasopoulos, J. Blake and B. E. Hayden, *J. Phys. Chem. C*, 2011, **115**, 19226–19230.
6 Y. Liu, G. Yu, G. Li, Y. Sun, T. Asefa, W. Chen and X. Zou, *Angew. Chem., Int. Ed.*, 2015, **54**, 10752–10757.
7 S. Q. Gong, Z. J. Jiang, P. H. Shi, J. C. Fan, Q. J. Xu and Y. L. Min, *Appl. Catal., B*, 2018, **238**, 318–327.
8 T. Wu, Y. Ma, Z. B. Qu, J. C. Fan, Q. X. Li, P. H. Shi, Q. J. Xu and Y. L. Min, *ACS Appl. Mater. Interfaces*, 2019, **11**, 5136–5145.
9 X. Wang, Q. X. Li, P. H. Shi, J. C. Fan, Y. L. Min and Q. J. Xu, *Small*, 2019, 1901530.
10 K. X. Liao, S. T. Chen, H. H. Wei, J. X. Fan, Q. J. Xu and Y. L. Min, *J. Mater. Chem. A*, 2018, **6**, 23062–23070.
11 J. Shi, R. Tong, X. Zhou, Y. Gong, Z. Zhang, Q. Ji, Y. Zhang, Q. Fang, L. Gu, X. Wang, Z. Liu and Y. Zhang, *Adv. Mater.*, 2016, **28**, 10664–10672.
12 J. Shi, Q. Ji, Z. Liu and Y. Zhang, *Adv. Energy Mater.*, 2016, **6**, 1600459.
13 G. Ye, Y. Gong, J. Li, B. Li, Y. He, S. T. Pantelides, W. Zhou, R. Vajtai and P. M. Ajayan, *Nano Lett.*, 2016, **16**, 1097–1103.
14 Z. Lu, W. Zhu, X. Yu, H. Zhang, Y. Li, X. Sun, X. Wang, H. Wang, J. Wang, J. Luo, X. Lei and L. Jiang, *Adv. Mater.*, 2014, **26**, 2683–2687.
15 J. Deng, H. Li, S. Wang, D. Ding, M. Chen, C. Liu, Z. Tian, K. S. Novoselov, C. Ma, D. Deng and X. Bao, *Nat. Commun.*, 2017, **8**, 14430.
16 D. Voiry, M. Salehi, R. Silva, T. Fujita, M. Chen, T. Asefa, V. B. Shenoy, G. Eda and M. Chhowalla, *Nano Lett.*, 2013, **13**, 6222–6227.
17 B. Guo, K. Yu, H. Li, H. Song, Y. Zhang, X. Lei, H. Fu, Y. Tan and Z. Zhu, *ACS Appl. Mater. Interfaces*, 2016, **8**, 5517–5525.
18 S. Xu, D. Li and P. Wu, *Adv. Funct. Mater.*, 2015, **25**, 1127–1136.
19 T. F. Jaramillo, K. P. Jørgensen, J. Bonde, J. H. Nielsen and S. Horch, *Science*, 2007, **317**, 100–102.
20 J. Kibsgaard, Z. Chen, B. N. Reinecke and T. F. Jaramillo, *Nat. Mater.*, 2012, **11**, 963–969.
21 M. R. Gao, M. K. Y. Chan and Y. G. Sun, *Nat. Commun.*, 2015, **6**, 7493–7501.
22 J. Xie, H. Zhang, S. Li, R. Wang, X. Sun, M. Zhou, J. Zhou, X. Lou and Y. Xie, *Adv. Mater.*, 2013, **25**, 5807–5813.
23 D. Kong, H. Wang, J. J. Cha, M. Pasta, K. J. Koski, J. Yao and Y. Cui, *Nano Lett.*, 2013, **13**, 1341–1347.
24 R. M. Ding, M. C. Wang, X. F. Wang, H. X. Wang, L. C. Wang, Y. W. Mu and B. L. Lv, *Nanoscale*, 2019, **11**, 11217–11226.
25 P. D. Tran, T. V. Tran, M. Orio, S. Torelli, Q. D. Truong, K. Nayuki, Y. Sasaki, S. Y. Chiam, R. Yi, I. Honma, J. Barber and V. Artero, *Nat. Mater.*, 2016, **15**, 640–646.
26 J. Kibsgaard, T. F. Jaramillo and F. Besenbacher, *Nat. Chem.*, 2014, **6**, 248–253.
27 L. R. L. Ting, Y. Deng, L. Ma, Y. J. Zhang, A. A. Peterson and B. S. Yeo, *ACS Catal.*, 2016, **6**, 861–867.
28 Y. H. Choi, J. Cho, A. M. Lunsford, M. Al-Hashimi, L. Fang and S. Banerjee, *J. Mater. Chem. A*, 2017, **5**, 5129–5141.
29 D. N. Nguyen, L. N. Nguyen, P. D. Nguyen, T. V. Thu, A. D. Nguyen and P. D. Tran, *J. Phys. Chem. C*, 2016, **120**, 28789–28794.
30 B. Lassalle-Kaiser, D. Merki, H. Vrubel, S. Gul, V. K. Yachandra, X. Hu and J. Yano, *J. Am. Chem. Soc.*, 2015, **137**, 314–321.
31 Y. H. Chang, C. T. Lin, T. Y. Chen, C. L. Hsu, Y. H. Lee, W. Zhang, K. H. Wei and L. J. Li, *Adv. Mater.*, 2013, **25**, 756–760.
32 K. Du, L. Zheng, T. Wang, J. Zhuo, Z. Zhu, Y. Shao and M. Li, *ACS Appl. Mater. Interfaces*, 2017, **9**, 18675–18681.
33 Y. Shang, X. Xu, B. Gao and Z. Ren, *ACS Sustainable Chem. Eng.*, 2017, **5**, 8908–8917.
34 T. R. Hellstern, J. Kibsgaard, C. Tsai, D. W. Palm, L. A. King, F. Abild-Pedersen and T. F. Jaramillo, *ACS Catal.*, 2017, **7**, 7126–7130.
35 S. Y. Gao, B. Wang, X. Y. Liu, Z. H. Guo, Z. Q. Liu and Y. C. Wang, *Nanoscale*, 2018, **10**, 10288–10295.

36 X. F. Zhou, S. H. Lin, X. L. Yang, H. N. Li, M. N. Hedhili, L. J. Li, W. J. Zhang and Y. M. Shi, *Nanoscale*, 2018, **10**, 3444–3450.
37 J. Zhang, T. Wang, D. Pohl, B. Rellinghaus, R. Dong, S. Liu, X. Zhuang and X. Feng, *Angew. Chem., Int. Ed.*, 2016, **55**, 6702–6707.
38 H. Wang, C. Tsai, D. Kong, K. Chan, F. Abild-Pedsersen, J. K. NØrskov and Y. Cui, *Nano Res.*, 2015, **8**, 566–575.
39 D. Wang, X. Zhang, Y. Shen and Z. Wu, *RSC Adv.*, 2016, **6**, 16656–16661.
40 Z. Xing, X. Yang, A. M. Asiri and X. Sun, *ACS Appl. Mater. Interfaces*, 2016, **8**, 14521–14526.
41 D. Merki, H. Vrubel, L. Rovelli, S. Fierro and X. Hu, *Chem. Sci.*, 2012, **3**, 2515–2525.
42 Y. Luo, X. Li, X. Cai, X. Zou, F. Kang, H.-M. Cheng and B. Liu, *ACS Nano*, 2018, **12**(5), 4565–4573.
43 J. Cao, J. Zhou, Y. Zhang, Y. Wang and X. Liu, *ACS Appl. Mater. Interfaces*, 2018, **10**(2), 1752–1760.
44 W. Lu, Y. Song, M. Dou, J. Ji and F. Wang, *Int. J. Hydrogen Energy*, 2018, **43**(18), 8794–8804.
45 X. N. Wang, R. Tong, Y. Wang, H. L. Tao, Z. H. Zhang and H. Wang, *ACS Appl. Mater. Interfaces*, 2016, **8**, 34270–34279.
46 R. Chen, C. Yang, H. Y. Wang, J. Miao, L. Zhang, S. Chen and B. Liu, *ACS Energy Lett.*, 2017, **2**, 1070–1075.
47 G. Kresse and J. Furthmuller, *Phys. Rev. B: Condens. Matter Mater. Phys.*, 1996, **54**, 11169–11186.
48 J. P. Perdew, K. Burke and M. Ernzerhof, *Phys. Rev. Lett.*, 1996, **77**, 3865–3868.
49 W. G. Fateley, F. R. Dollish, N. T. McDevitt and F. F. Bentley, *Infrared and Raman Selection Rules for Molecular and Lattice Vibrations: The Correlation Method*, Wiley Interscience, New York, 1972, pp. 78–212.
50 Z. Cheng, H. Abernathy and M. Liu, *J. Phys. Chem. C*, 2007, **111**, 17997–18000.
51 M. Placidi, M. Dimitrievska, V. Izquierdo-Roca, X. Fontané, A. Castellanos-Gomez, A. Pérez-Tomás, N. Mestres, M. Espindola-Rodriguez, S. López-Marino, M. Neuschitzer, V. Bermudez, A. Yaremko and A. Pérez-Rodríguez, *2D Mater.*, 2015, **2**, 035006.
52 J. Li, S. Wang, T. Xiao, X. Tan, P. Xiang, L. Jiang, C. Deng, W. Li and M. Li, *Appl. Surf. Sci.*, 2017, **420**, 919–926.
53 C. Tsai, K. Chan, J. K. Norskov and F. Abild-Pedersen, *Surf. Sci.*, 2015, **640**, 133–140.
54 B. E. Conway and B. V. Tilak, *Electrochim. Acta*, 2002, **47**, 3571–3594.
55 Y. Yu, G. Nam, Q. He, X. Wu, K. Zhang, Z. Yang, J. Chen, Q. Ma, M. Zhao, Z. Liu, F. Ran, X. Wang, H. Li, X. Huang, B. Li, Q. Xiong, Q. Zhang, Z. Liu, L. Gu, Y. Du, W. Huang and H. Zhang, *Nat. Chem.*, 2018, **10**, 638–643.
56 L. Feng, G. Yu, Y. Wu, G. Li, H. Li, Y. Sun, T. Asefa, W. Chen and X. Zou, *J. Am. Chem. Soc.*, 2015, **137**, 14023–14026.
57 I. Roger, R. Moca, H. N. Miras, K. G. Crawford, D. A. J. Moran, A. Y. Ganin and M. D. Symes, *J. Mater. Chem. A*, 2017, **5**, 1472–1480.
58 H. Li, C. Tsai, A. L. Koh, L. Cai, A. W. Contryman, A. H. Fragapane, J. Zhao, H. S. Han, H. C. Manoharan, F. Abild-Pedersen, J. K. Nørskov and X. Zheng, *Nat. Mater.*, 2016, **15**, 48–53.
59 D. Wang, X. Zhang, Y. Shen and Z. Wu, *RSC Adv.*, 2016, **6**, 16656–16661.
60 J. Hu, C. Zhang, L. Jiang, H. Lin, Y. An, D. Zhou, M. K. H. Leung and S. Yang, *Joule*, 2017, **1**, 1–11.
61 Y. Wu, G. Li, Y. Liu, L. Yang, X. Lian, T. Asefa and X. Zou, *Adv. Funct. Mater.*, 2016, **26**, 4839–4847.
62 J. Zhang, T. Wang, P. Liu, S. Liu, R. Dong, X. Zhuang, M. Chen and X. Feng, *Energy Environ. Sci.*, 2016, **9**, 2789–2793.